Flows, Transport, and Effective Drag in Intertidal Salt Marsh Creeks

Collin Ortals[1], Orlando Cordero[2], Arnoldo Valle-Levinson[1], and Christine Angelini[1,3]

[1]Department of Civil and Coastal Engineering, University of Florida, Gainesville, FL, USA, [2]Department of Geological Sciences, University of Florida, Gainesville, FL, USA, [3]Department of Environmental Engineering Sciences, University of Florida, Gainesville, FL, USA

Abstract Intertidal creeks (channel width <5 m) weave through salt marshes, delivering water, nutrients, and sediments into the marsh interior and affecting spatial heterogeneity in plant and animal distributions. Despite their global prevalence, creek connectivity, and the mechanisms controlling cross-marsh hydrodynamics, remain poorly resolved. In this study, we measured flow and total suspended solids transport in three intertidal creeks within a confined drainage basin in a Georgia, USA salt marsh. We discovered that the effective drag is 3–12 times greater than bed drag, reaching levels similar to those observed in coral reefs. Furthermore, the drag between tidal flood and ebb phases differs, indicating an asymmetric drag. Analyses of along-channel momentum reveal that pressure gradient $O\left(10^{-3}-10^{-2}\right)$ m/s and friction $O\left(10^{-3}-10^{-2}\right)$ m/s² dominate creek momentum balance. Divergence in tidal and suspended solids transport between adjacent creeks revealed contrasting tidal transport asymmetries (i.e., flood or ebb dominated) within this confined basin. We discuss how these differences may alter the eco-geospatial evolution of salt marshes and their response to sea-level rise.

Plain Language Summary Salt marshes generate a valuable suite of ecological and economic services. Key to understanding their fate in relation to rising sea levels is understanding the eco-physical dynamics of the creeks that weave through these marshes, as these features serve as major conduits of water, sediments, and biological material exchange. Models have been developed to explain how flow moves through creeks over one tidal cycle. However, there are limited field measurements resolving the dominant forms of drag controlling tidal fluxes through creeks, divergences in water flow and sediment transport between creeks, or creek-creek circulations. This study applies field measurements from a Georgia salt marsh to address these knowledge gaps. We discover that adjacent creeks in a confined drainage basin are governed by form drag produced by flow interactions with the landscape and vegetation and exhibit profound heterogeneity in tidal flows and sediment transport. We highlight that this local-scale heterogeneity likely plays a major role in altering the pattern and mechanisms by which salt marshes are responding to sea-level rise.

1. Introduction

1.1. Salt Marshes and Tidal Creeks

Salt marshes form along temperate, low-energy coastlines worldwide where they provide valuable ecological (e.g., C-sequestration, N-cycling, and biodiversity enhancement) and economic services (e.g., fisheries and storm surge reduction) (Barbier et al., 2011; Bouma et al., 2014; Temmerman et al., 2013). These tidally flooded landforms are created via sedimentation, a process that is enhanced by vegetation (Fagherazzi et al., 2012). The feedbacks that occur between water flow, vegetation, and sedimentation allow salt marshes to adjust in vertical relief and spatial extent in response to sea-level changes and shorter timescale events—such as hurricanes, droughts, and oil spills (Coverdale et al., 2012; Fagherazzi et al., 2012; Lin & Mendelssohn, 2012). Within these biogenic coastal landforms, tidal channels and creeks bisect elevated marsh platforms, forming branched networks that control the exchange of water (Bayliss-Smith et al., 1979; Boon, 1975; French & Stoddart, 1992; Healey et al., 1981; Hughes, 2012; Mariotti & Fagherazzi, 2011), sediments (Christiansen et al., 2000; Voulgaris & Meyers, 2004), and suspended biological material between the estuary and marsh interior (Struyf et al., 2013).

Supervision: Collin Ortals, Christine Angelini
Validation: Collin Ortals, Arnoldo Valle-Levinson
Visualization: Collin Ortals, Orlando Cordero, Arnoldo Valle-Levinson, Christine Angelini
Writing – original draft: Collin Ortals, Orlando Cordero, Christine Angelini
Writing – review & editing: Collin Ortals, Orlando Cordero, Arnoldo Valle-Levinson, Christine Angelini

Previous research has focused on understanding water flow and sediment transport in subtidal channels with widths between 10 and 1000s of meters. However, few studies have examined flows in intertidal creeks with widths smaller than 10s of meters. This is despite the ubiquity of intertidal creeks in salt marshes and their propensity to both modify flow and sedimentation patterns, and control the fitness and distribution of plants and animals across marsh landscapes (Pieterse et al., 2012, 2015).

In this study, field measurements are analyzed to address three gaps in the literature related to intertidal creek (<5 m wide) flows and sediment transport: (a) What is the in-channel behavior of velocities in multiple tidal creeks in a confined drainage basin? (b) What are the sources and influences of effective drag and bed drag in tidal creeks?, and (c) What are the mechanisms underlying creek connectivity and cross-marsh circulations, and how do they depend on tidal phase? We summarize these knowledge gaps in the sections below and focus our field measurements on a Georgia (USA) salt marsh.

1.2. Velocities in Multiple Tidal Creeks in a Confined Drainage Basin

A simplified model by Boon (1975) explained the tidal stage-velocity (discharge) asymmetry (differences in velocity [discharge] at the same tidal stage for different phases of the tide) in a tidal creek. Boon's observational data showed marked differences in velocity between phases of the tide, which in part, was explained by incorporating quarter-diurnal and sixth-diurnal harmonics into the tidal model. When compared to model output simulated only with the fundamental harmonic (semi-diurnal), flood/ebb discharge peaks occurred at different times, and with increased magnitude. While this model helped explain general patterns in differences of velocity between flood and ebb, it could not fully reproduce the tidal velocity asymmetries, and in particular, the surge effect on ebb tides at below-bank elevations, or when outflow concentrates through the channel, without overbank flow (Fagherazzi et al., 2008). This was due to key limiting assumptions, namely that the model did not consider wind stresses and assumed that: (a) the water surface is "flat" (i.e., no water level slopes), (b) the system is frictionless (i.e., water disperses throughout the system instantaneously), and (c) all flow passes through the channel section (i.e., no overbank flow). Subsequent studies identified the need to include the role of overbank flow (French & Stoddart, 1992), which could account for 0%–60% of the water budget in a marsh (Temmerman et al. (2005). The percentage of the water budget attributed to overflow depended on tidal amplitude and environmental conditions, such as wind forcing. Fagherazzi et al. (2008) expanded the Boon model by incorporating a constant linearized friction term on the landscape with the tidal instantaneous geomorphologic elementary response (TIGER) model. In the TIGER model, water surface elevation gradients on the marsh are estimated through Poisson's Equation which considers average water depth, the friction coefficient, and change in stage of the tidal inlet. Furthermore, time-varying infilling and outflowing were accounted for by estimating travel time distributions in both channels and on the marsh platforms. Their model was able to capture the time-lag effects of tidal flow asymmetries previously uncaptured by the Boon model. However, the data used to validate these models were limited to field measurements of a single creek. Thus, it is unclear whether the models are able to resolve potential interactions between multiple adjacent creeks.

1.3. Sources and Effects of Tidal Creek Drag

Drag is caused by different features in coastal landscapes, including bed composition (Grant & Madsen, 1982; Nikuradse, 1933), topographic roughness (Monismith, 2007; Warner & MacCready, 2014), channel morphology (Bo & Ralston, 2020; Kranenburg et al., 2019; Li et al., 2004), and vegetation (Horstman et al., 2021; Monismith et al., 2019; Nepf, 1999). Frictional drag has been characterized in various forms such as friction factors (i.e., Darcy-Weisbach) or coefficients (i.e., Manning's n) (Yen, 2002) or non-dimensional quadratic drag coefficients (Bo & Ralston, 2020). A source of drag in marsh landscapes can be bed drag, which results from fluid flow and bed interactions that form a boundary layer at the interface. These interactions result in the characteristic logarithmic velocity profiles for fluids (Equation 1),

$$u(z) = \frac{u_*}{\kappa}\left[\ln\left(\frac{z-d}{z_0}\right)\right] + \beta \tag{1}$$

whereby the magnitude of bed drag generally scales with the bed roughness height z_0 (Nikuradse, 1933) or with the size of bedforms (Grant & Madsen, 1982). In Equation 1, $u(z)$ is the fluid velocity at reference height z above the bed, κ is the von Karman's constant $(= 0.41)$, u_* is the shear velocity at z, d is the local water depth, z_0 is a bottom roughness length scale, and β is a correction coefficient, or residual. Bottom drag is often expressed in terms of a dimensionless coefficient, $C_{d,bot}$ (Voulgaris & Meyers, 2004) and can be related to the roughness length scale using:

$$z_o = z\, exp\left(-\kappa\, /\, \left(C_{d,bot} \right)^{\frac{1}{2}} \right)$$ (2)

Note that the bottom drag coefficient is typically referred to as C_d in literature, however, in this study, it is referenced as $C_{d,bot}$ to distinguish from other types of drag considered. The bed drag coefficient for a flow with negligible transverse component can be obtained using the following relationships:

$$\tau = \rho u_{*,bot}^2$$ (3)

$$\tau = \rho \left(C_{d,bot} \right) u_z^2$$ (4)

where τ is the bed shear stress and u_z is the reference streamwise velocity.

Additionally, drag can be evaluated in terms of effective drag, caused by different features in the landscape, such as vegetation or reefs. This is often expressed in the form of the dimensionless drag coefficient, $C_{d,eff}$, which is the ratio, or balance, between driving and restoring forces in the momentum equation (Horstman et al., 2021; Kranenburg et al., 2019; Li et al., 2004; Monismith, 2007). In controlled laboratory settings, the drag effects from various features (e.g., vegetation) can be isolated (Nepf, 1999). In field settings, however, it is infeasible to isolate the different contributing factors (i.e., vegetation, bed and microtopography effects). Therefore, it is useful to express drag as a bulk term, or the "integrated effects" of the landscape (Monismith et al., 2019). Efforts have been made to estimate the drag effects from reefs which have been found to be up to 10× greater than the canonical 0.0025 value for muddy or sandy sea beds (Monismith, 2007). Furthermore, Monismith et al. (2019) found that the drag from seagrass beds can range from 0.05 to 1 depending on the phase of the tide.

Herein, $C_{d,bot}$ is defined as drag resulting from flow interactions with bed material and bedforms and $C_{d,eff}$ is defined as the "integrated" drag resulting from flow interactions with the landscape, channel morphology, and vegetation. In this study, $C_{d,eff}$ is reported as a function of water level and phase at two intertidal salt marsh creeks. This study also describes the importance of effective drag relative to bed drag in these systems. Understanding their relative importance is necessary for resolving the controlling mechanisms of flow and transport in salt marsh creeks as well as to understanding how vegetation and other landscape features may modulate flow during different stages of the tide.

1.4. Creek-To-Creek Flow Interactions and Overmarsh Circulations

Torres et al. (2007) conducted a field campaign to quantify overmarsh circulation and creek flows. Their study revealed that regular exchanges of water occur at the heads of tidal creeks, meaning water may enter and exit the system in different creeks (i.e., where tidal creeks terminate in marsh platforms). They suggested that drainage basins, or divides, are not clearly or consistently delineated during high water events within salt marshes, a pattern contrary to well-defined, temporally stable divides in fluvial systems. Using numerical simulations of marsh circulation in which first-order and second-order tidal creeks were systematically removed from a high-resolution digital elevation model (resulting in a <60% reduction of drainage density), Sullivan et al. (2019) discovered that such creek removal did not affect large-scale circulation and tracer dispersal. However, following the removal of third-order and fourth-order creeks as well (an up to 85% reduction of drainage density), the authors discovered that the system transitioned from being ebb-dominated to flood-dominated. This transition was caused by losses in hydraulic conductivity and in the ability of tidal creeks to convey water further into the marsh platform interior. While small intertidal creeks may not control kilometer-scale overmarsh circulations as this study concludes (Torres & Styles, 2007), it is unclear
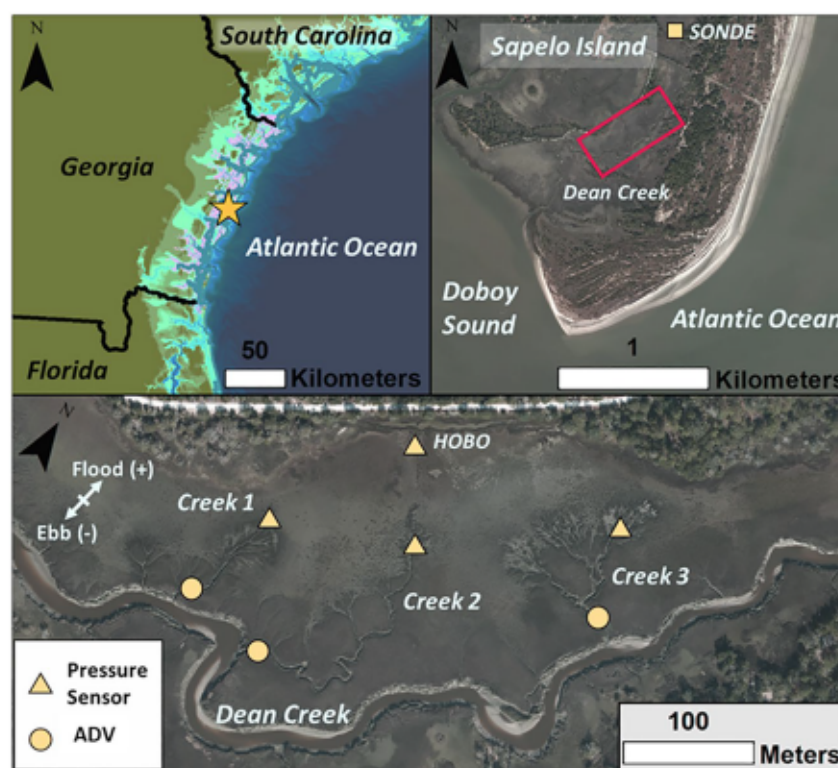
Figure 1. Overview of study site, including the location of Sapelo Island (star) within the South Atlantic Bight (a) (background map is from the NOAA Coastal Relief Model), the Dean Creek marsh-creek system on the southern end of Sapelo Island (b) (background image is 2017 aerial imagery by the Georgia Coastal Ecosystem LTER), and the location of our field study area, deployed instruments (pressure sensors highlighted as yellow triangles, and Vectors (ADVs) as yellow circles), and naming convention for creeks referred to throughout the study (c) (same background image as (b)). Note that the data frame in (c) is rotated from north (as denoted in red box panel (b)).

whether creek-creek flow interactions lead to limited inflow or early flow reversals of adjacent creeks. Such creek dynamics have the potential to alter residence times, sedimentation, and the transport of material.

2. Materials and Methods

2.1. Field Site Characteristics

To address the three aforementioned knowledge gaps pertaining to in-channel behavior velocities of multiple tidal creeks, sources and influences of drag, and mechanisms underlying creek connectivity, we conducted a field study on Sapelo Island, Georgia, USA, within the South Atlantic Bight (SAB) (Figure 1a), a region dominated by semi-diurnal tides. The tidal amplitude in this area ranges from ~0.5 to 1.6 m over the neap-spring tidal period. The coastal region in this area is characterized by barrier islands and intertidal wetlands (ranging from freshwater, brackish, and salty) along the estuarine gradient fed by major tributaries, namely the Ogeechee River, Blackbeard Creek, Altamaha River, and Satilla River. At the study site, the salt marsh is dominated by monocultures of *Spartina alterniflora*, a C4 grass that ranges in height from 0.3 to 0.5 m in higher elevation marsh platforms and can exceed 2 m in lower creekbank elevations. Pinton et al. (2020) provide detailed estimates of *S. alterniflora* stem height and density derived from UAV LiDAR in a nearby marsh where the vegetation spatial distribution and abundance follow a similar pattern as the Dean Creek study site.

The sampling site, a marsh area fed by Dean Creek on the southern tip of Sapelo Island (Figures 1b and 1c), is located within the Sapelo Island National Estuarine Research Reserve (SINERR), which operates long-term ecological and hydrological monitoring stations as a part of the U.S. NERR System-Wide Monitoring Program.

Dean Creek and its surrounding intertidal salt marshes are bordered to the east by an upland forested relic dune system (driven by island migration), to the north by a road and bridge leading to the beach, and to the west by another road built along a hammock, or relic barrier shoreline. The southern end of Dean Creek is connected to the Doboy Sound, near to the Atlantic Ocean (roughly 1.2 km inland). The focal marsh area is approximately 0.52 km² (52.3 hectares). The segment of Dean Creek in the domain is approximately 2.1 km long and, on average, approximately 20 m wide, and has an average sinuosity of 1.5 (sinuosity defined in Finotello et al., 2018). The study site (outlined in red Figure 1b) is 1–1.5 km upstream of the confluence between Dean Creek and the Doboy Sound.

The focal drainage basin (0.07 km² or 7.45 hectares) at the study site (Figure 1c, note that map is rotated from north), is primarily fed by three intertidal creeks (channel widths <5 m), herein referred to by their naming convention—Creeks 1, 2, and 3—labeled in the map. The creekmouth bed elevation of each creek is approximately −0.57, −0.53, and −0.94 m above mean sea level (m.a.m.s.l.), respectively (Figure 2). Details regarding each creeks' geomorphic characteristics are in Table 1. The low marsh elevation varies from ~0.6 to 0.8 m.a.m.s.l. at the site, with higher levees along Dean Creek's channel banks reaching elevations of 1.15 m.a.m.s.l., a level equivalent to the local mean higher high water—MHHW (see Figure 2a).

2.2. Field Instrumentation

We deployed one Nortek Vector acoustic Doppler velocimeter (ADV) in each of three adjacent tidal creeks within a contiguous salt marsh fed by Dean Creek on Sapelo Island, Georgia (31°23'22.88"N, 81°16'29.07"W, see Figure 1 for map of instrument array and tidal creek naming convention). Each ADV was deployed 5–10 m upstream of each creekmouth by mounting the instrument to a steel frame that included a crossbar that spanned the tidal creek; a bubble level was used to ensure the ADVs were mounted vertically with the sensors facing down. The ADVs measured both three-dimensional velocities and pressure. Sampling volumes were 20, 30, and 30 cm above the bed for Creeks 1, 2, and 3, respectively. We paired each ADV with an RBR SoloD Fast8 pressure sensor (herein referred to as pressure sensor) which was positioned upstream of each ADV. The streamwise distances between each ADV and its paired pressure sensor were 85, 220, and 110 m for Creeks 1, 2, and 3, respectively. The pressure sensors were mounted to a metal T-post which was driven into the marsh until resistance was met. A HOBO pressure sensor was mounted adjacent to Lighthouse Road in air, approximately 2.5 m.a.s.l., to capture the local atmospheric pressure variations. All instrument positions were surveyed on the same day to UTM 17N coordinate system and the local mean sea level vertical datum with a Trimble Geo7x RTK-GPS (vertical error is ±2 cm) and exported using Trimble Pathfinder Office. In this region, the vertical datum NAVD88 can be related to local mean sea level by subtracting 12.3 cm (vertical uncertainty is ± 6.87 cm, https://vdatum.noaa.gov/vdatumweb). The ADVs were set to record in continuous mode at 32 Hz for the duration of the experiment. The pressure recorded at a sampling frequency of 8 Hz, and the HOBO recorded at 1 Hz. All data recordings when the instruments were not submerged during low tide were discarded. A total of 20 tidal cycles were captured for all instruments. The start and end dates of the study were July 25, 2019 to August 5, 2019, which is during peak productivity periods of *S. alterniflora*.

During the study period, at a nearby weather station, the average wind speeds recorded were 2.7 m/s with maximum winds up to 8.6 m/s. The wind direction was generally from the north except for July 26, when the winds were from the northeast (additional sensor information can be found at: http://gce-lter.marsci.uga.edu/portal/stations/sinerr/).

2.3. Data Post-Processing

2.3.1. Water Levels

Water levels (referred to in meters above local mean sea level) for ADVs and pressure sensors (RBRs) were computed by subtracting out the local atmospheric pressure measured by the HOBO, converting to water depth, and then adding the reference elevation value taken with an RTK. To assess the along channel pressure (water surface) slopes, we made small vertical adjustments in computed water levels at the pressure sensors such that the gradient would be zero when the ADV measured zero flow (due to small vertical errors in survey equipment measurements, <3 cm). Then we used Creek 2 water level as our fixed reference and
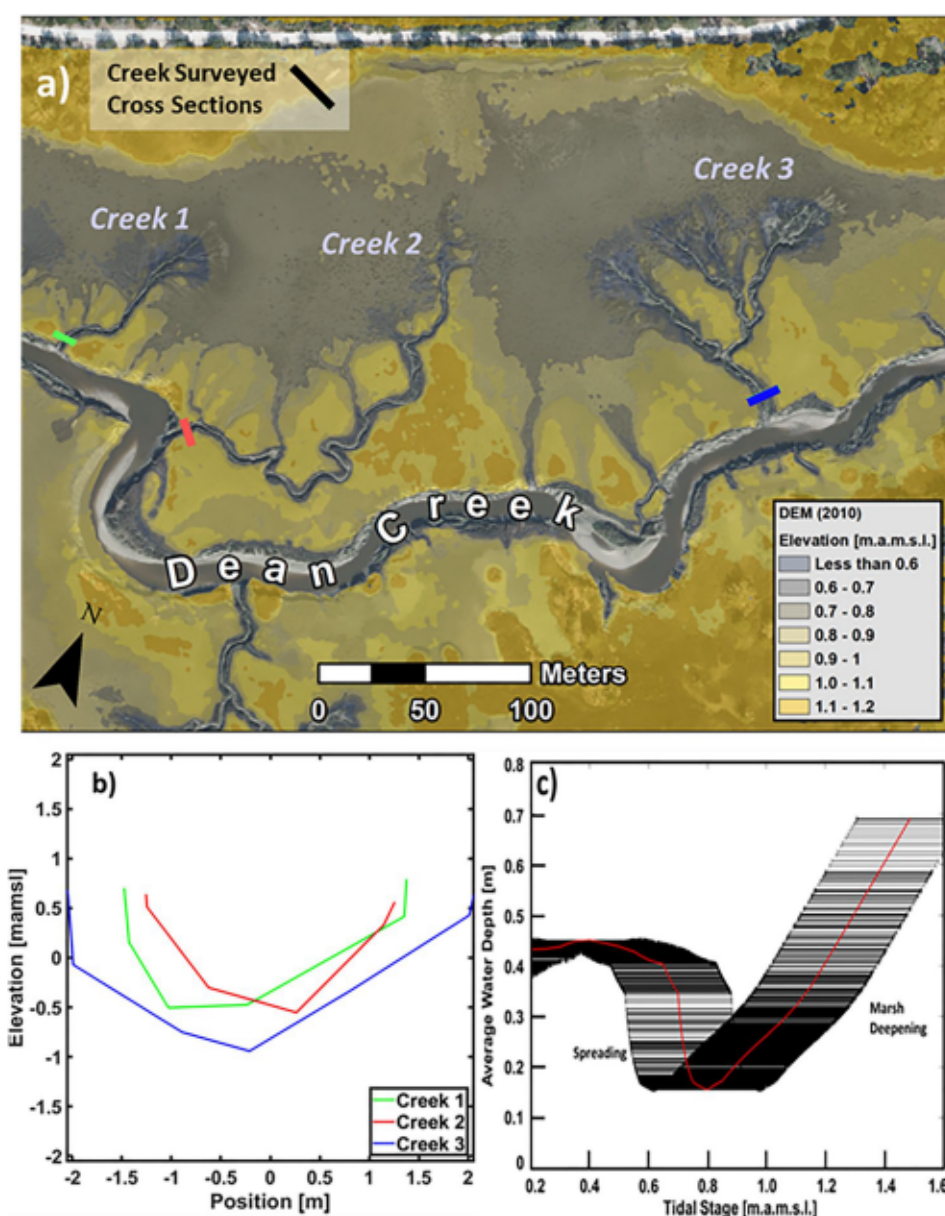
Figure 2. Digital elevation model (DEM) from NOAA 2010 LiDAR (Office for Coastal Management, 2010), (b) RTK surveyed creek cross-sections, and (c) estimated average water depth determined from low to high stages (x-axis) DEM of the study area. The estimated water depth assuming a "flat" water surface at different tidal stages and assessing the average depth within the study domain. Black horizontal lines represent vertical uncertainty in DEM elevation Note that for a lower stage the average depth can be higher due to less marsh surface area being flooded.

Table 1
Creek Characteristics (2006–2016)

Creek ID	Type	Creek length (L) (m)	Creek sinuosity	ΔL (m/y)	% change L	XS flow area range (m²)	Hydraulic radius range (m)	Confluence location[a]	Confluence orientation[a]
Creek 1	Single threaded	100	1.1	2	25	0.75–4.6	0.3–1.0	Straight-away	Normal
Creek 2	Single threaded	270	1.7	0.5	2	0.89–4.0	0.35–1.0	Bend apex[b]	Coincident
Creek 3	Reticulated	130[c]	–	1.4	–	1.17–7.5	0.36–1.28	Straight-away	Normal

[a]Relative to main channel. [b]Main Channel bend (W/R) = 0.8. [c]Longest reticulated segment.

assumed that, at high water measured for each pressure sensor (marsh platform), each sensor would have the same peak water surface elevation. Additionally, we evaluated the cross-marsh water surface slopes (from Creek 1 pressure sensor to Creek 3 pressure sensor). The precision for pressure measurements is 0.01 dbar for the RBRs and 0.01 dbar for the ADVs, which translates to ~1 cm precision in depth.

2.3.2. Acoustic Doppler Velocimeters

A low signal-to-noise ratio (SNR) in acoustic instruments, or the ratio of instrument signal intensity compared to the instrument background noise level, can be caused by low concentration of particles, or "scatterers," in the water column (Voulgaris & Trowbridge, 1998). In marsh systems, this can occur during slack tide when water velocities are slow or close to zero, and particles have had time to settle in the water column. As recommended by the manufacturer for Nortek Vectors (Rusello, 2009), we applied a cutoff of 30 SNR where velocity measurements below the threshold were removed and replaced with a 5-min windowed mean value (i.e., averaged 2.5 min prior and 2.5 min post replacement measurement).

Velocity spikes were removed following the approach of Goring and Nikora (2002) through a 12-point cubic spline. As the cubic spline produced large values, we used a local mean value. The spikes were identified using the phase-space method (Goring & Nikora, 2002) and a 5-min window, or $N=9,600$ samples. After accounting for spikes, velocities were rotated to represent the streamwise (u), cross-stream (v), and vertical (w) axes for each channel. Positive (+) streamwise values in subsequent analyses represent flood phases and negative (−) represents ebb.

2.3.3. Estimating Bottom and Effective Drag Coefficients

ADVs have successfully been used to estimate quadratic bottom drag coefficients in various coastal and estuarine environments including in estuaries with mud flats, tidal channels, and wave breaking zones (Blanton et al., 2004; Feddersen et al., 2003; Horstman et al., 2021; Nidzieko & Ralston, 2012; Voulgaris & Meyers, 2004). The bottom drag coefficient $C_{d,bot}$ depends on the bottom roughness height z_0 (Nikuradse, 1933) or bedforms (Grant & Madsen, 1982) (Equations 1–3). This is a key parameter in understanding vertical variation in velocity, or the shear stresses, which determine bed erosion. ADVs have been found to accurately measure turbulent velocity fluctuations, where the cross-correlation of the horizontal and vertical components can predict the shear velocity in the Reynolds Stress Method (Soulsby, 1983) (Equations 5 and 6).

$$u_{*,z} = \left(\langle u'w' \rangle^2 + \langle v'w' \rangle^2 \right)^{1/4} \tag{5}$$

$$u_{*,bot}^{\,2} = \frac{u_{*,z}^{\,2}}{1 - \dfrac{z}{d}} \tag{6}$$

$$C_{d,bot} = u_{*,bot}^{\,2} / u_z^{\,2} \tag{7}$$

where $u_{*,z}$ is the shear velocity at elevation z above the bed, u', v', and w' are the deviations from a time average velocity denoted by brackets and representing 5-min data sets, and d is the local water depth. The drag can then be estimated as the best fit line of data (Equation 7). Voulgaris and Meyers (2004) found sensor misalignment from the vertical may lead to underestimation in bottom shear velocity estimates (up to 15% in their study) compared to the inertial dissipation method (Kim et al., 2000). However, this error is relatively small when compared to uncertainty in subsequent effective drag estimates (Figure 6 shaded regions mean ± 1 local standard deviation). In addition, the effective drag (form + bottom drag) allows understanding on how the integrated effects of bathymetry (e.g., Monismith, 2007; Warner & MacCready, 2014) or vegetation (e.g., Monismith et al., 2019; Nepf, 1999) alter water flow and sediment transport. Effective drag values for tidal creeks of this size (channel width <5 m) have not yet been estimated from field measurements and were assessed at each ADV location. We assume that water density is homogeneous, thus neglecting baroclinicity. We then used a one-dimensional streamwise x momentum equation:

$$\frac{\partial U}{\partial t} + U \frac{\partial U}{dx} = -g \frac{\partial \eta}{\partial x} - C_{d,eff} \frac{U\,U}{R_h} \tag{8}$$

where U is the cross-sectionally averaged streamwise velocity, x is the along-channel distance, η is the water surface elevation, and R_h is the hydraulic radius (section flow area A over the section wetted perimeter P). Due to a limited number of instruments, we replace U with u_z, the locally measured velocity at each ADV, as we could not resolve the cross-channel velocity structure with our instrument array. We anticipate that the consequence of replacing U with u_z results in an underestimate of $C_{d,eff}$, as u_z is higher in value than U (i.e., if u_z overestimated U by 20%, then $C_{d,eff}$ would be underestimated by 30%). From scaling and from measurements, $\frac{\partial u_z}{\partial t}$ is $O(10^{-4})$, so the terms on the left-hand side of Equation 8 are assumed to be small (i.e., time and length scales are much greater than the velocity) (Friedrichs & Madsen, 1992; LeBlond, 1978). Since the channel width is the same order of magnitude as the water depth, the hydraulic radius cannot be approximated as the water depth. Solving for $C_{d,eff}$, we have the following relationship:

$$C_{d,eff} = \frac{-g\frac{\Delta \eta}{\Delta x}}{\frac{u_z u_z}{R_h}} \qquad (9)$$

where $\frac{\Delta \eta}{\Delta x}$ is the along channel water surface gradient, computed with the RBR and ADV pressure measurements, and R_h was solved for different water depths using RTK survey measurements. The ratio of effective and bed drag, $C_{d,eff} / C_{d,bot}$, represents the proportion of effective drag relative to bed drag which reduces to the following relationship (ratio of Equations 7 and 9):

$$\frac{C_{d,eff}}{C_{d,bot}} = g\frac{A}{P}\frac{\frac{\Delta \eta}{\Delta x}}{u_*^2} \qquad (10)$$

which indicates that as the water depth approaches 0 (and hydraulic radius becomes small) then $C_{d,eff} / C_{d,bot} \rightarrow 1$ meaning the total drag is due to the bed. Values of $C_{d,eff} / C_{d,bot} \gg 1$ indicate that drag from other sources dominate frictional effects. Note that Creek 1 was not included in the analysis of bed and effective drag due to the sensitivity of these calculations with respect to instrument vibrations which appeared to have occurred as indicated by less reliable estimates of the drag (i.e., sensitive due to correlation of fluctuation terms and sensitivity to gradient measurements in effective drag).

2.3.4. Tidal Transport

Tidal exchange was estimated for each creek and for each tidal cycle. The tidal exchange is approximated in each channel by first estimating the mean streamwise velocity using the von Karman-Prandtl equation (Equation 1) by subdividing the profile over $N = 50$ vertical sigma layers (function of water depth at time t) (Dyer, 1971). z_0 was estimated from $z_0 = z \times \exp\left[-\kappa / \left(C_{d,bot}\right)^{1/2}\right]$ (Voulgaris & Meyers, 2004). Previous authors have suggested using a two-point method for fitting a logarithmic profile, that is, ADV or current meter placed at 0.2 d above bed and 0.8 d above bed where d is the total water depth (m) and then averaged (Walker, 1988). Due to instrument availability, we utilized one instrument for each location and estimated the vertical velocity profile, and used the computed depth-averaged velocity to be representative of the section (Rantz, 1982; Walker, 1988). While the velocity profile was assumed logarithmic, this may not necessarily be true in these locations. With lack of ground-truthing data for the velocity profile for this assumption, we can still test the robustness of our results. This is done by introducing a large factor of uncertainty in the depth-averaged velocity estimate (i.e., an increase or decrease of 33% in depth-averaged velocity). The uncertainty factor provides the sensitivity in net tidal transport estimates, which can be seen in Figure 6a (horizontal error bars) for the net tidal transport computation. Additionally, part of the tidal cycle is not captured due to instrument drying at lower tidal elevations. The missing components were estimated by assuming the rate at which the tidal stage rose or fell remained constant for the missing components, by which we estimated the time the water stage reached the first valid measurement (flood) and the time until the channel became dry (ebb). The missing velocities were linearly interpolated from the first (last) valid measurement and extended from or to zero (no flow when dry). For Creek 1 for all tides, the median value of missing components of net tidal transport was 2.7% (underestimating net outflow) compared to the measure portion of flow. For Creek 2, the median of the missing component was 24% (overestimating net
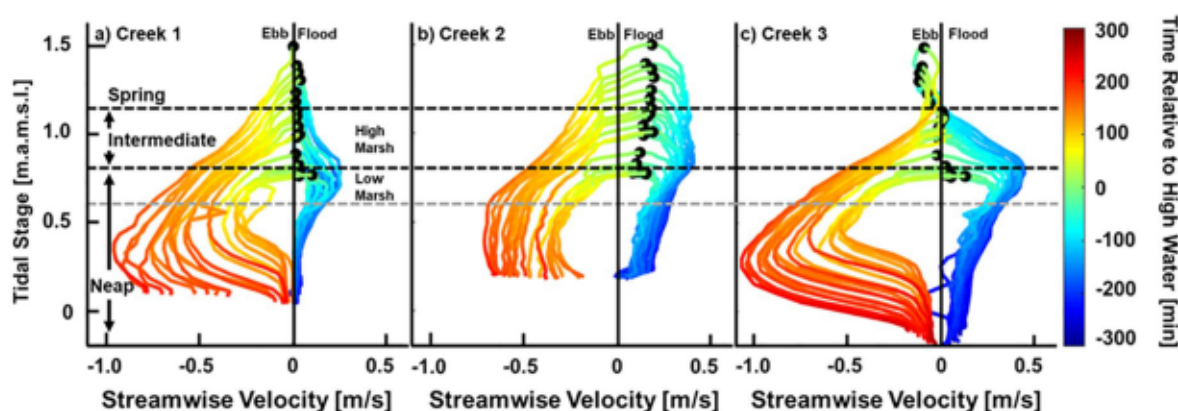
Figure 3. The stage-velocity (streamwise component) relationship for all available data from ADVs in Creek 1 (a), Creek 2 (b), and Creek 3 (c). Positive velocity values indicate tidal flooding and negative indicate ebbing. The colors indicate time (minutes) relative to Creek 2 high water ([−] is prior and [+] is after high water). Black circles denote the streamwise velocity at Creek 2 high water. The low marsh elevation range as well as local Mean Higher High Water (MHHW) are indicated by gray and black horizontal lines, respectively.

inflow). Finally, the median of Creek 3 was ~1% (underestimating net outflow). The estimated portion of missing tidal transport and introduction of a large uncertainty term (±33%) in mean channel flow value did not change the general pattern in net tidal fluxes.

2.3.5. TSS Transport

To estimate the total suspended sediments (TSS) in each creek, we collected water samples using bilge pumps mounted to T-posts at the same elevation as the ADV sampling volume and approximately 1 m upstream from each ADV. Samples were taken at 30-min intervals for 5 h over the course of one tidal cycle. All samples were kept on ice until transported to the lab, where they were filtered through Whatman Glass Fiber Filters (0.7 μm) and freeze-dried to remove moisture. Filter pre-weights were subtracted from post-weights and divided by the volume of water filtered for each sample. TSS exchanges were estimated by multiplying the concentration values and estimated tidal transport.

For subsequent analyses, we interpreted our data in three groupings based on tidal amplitude relative to approximate tidal creek bank elevation (0.8 m.a.m.s.l.) and MHHW estimated from the nearby NOAA Rockdedundy harmonic tidal prediction station (1.15 m.a.m.s.l.). For brevity, the zones are hereafter referred to as Neap (<0.8 m.a.m.s.l.), Intermediate (>0.8 and <1.15 m.a.m.s.l.), and Spring Tides (>1.15 m.a.m.s.l.). In addition, to compare across creeks, tidal times presented in subsequent figures are relative to Creek 2 high water as the three creeks experience high water at different times. High water differed between ~5 and 10 min (Creeks 1 and 2 occurring roughly the same time, and delayed at Creek 3).

3. Results

3.1. Time Variation of In-Channel Velocities and Water Surface Slopes

3.1.1. Neap Tides (Tidal Amplitude <0.8 m.a.m.s.l.)

All creeks showed the characteristic stage-velocity curve whereby the flow gradually increased during flood tide (+values) (Figures 3 and 4), peaking as the marsh platform is overtopped and then decreasing after the floodable area expands (Boon, 1975; Healey et al., 1981; Mariotti & Fagherazzi, 2011). On average, the creek flood velocities peaked 60–70 min before high water, at 0.15, 0.20, and 0.30 m/s in each creek, respectively. This time coincided with the overmarsh flooding, which during neap occurs only in localized areas adjacent to the creekheads (elevations were approximately 0.68 m.a.m.s.l.). At high water, all creeks continued to inflow, albeit <0.05 m/s in Creeks 1 and 3.Creek 2 continued to inflow at 0.11 m/s, roughly 2–3 times faster than the other creeks. Creek 2 showed slack water 25 min after high water, and roughly 10 min following the other creeks (black circles in Figure 3 or dashed vertical lines in Figure 4b). Peak ebb flow in Creek 1 occurred 92 min following high water, 30 min before Creeks 2 and 3.
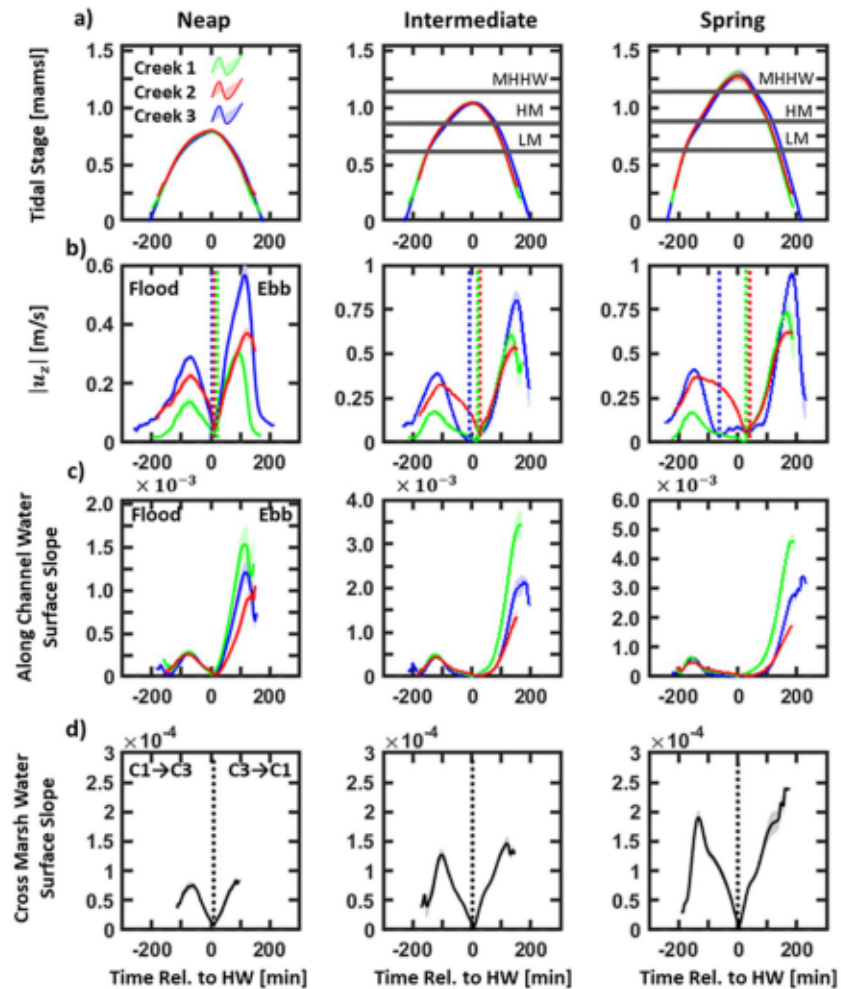
Figure 4. Ensemble averaged tidal stage measured at ADVs (a), streamwise water velocity magnitudes (b), along channel water surface slope (c), and cross marsh water surface slopes evaluated from pressure sensors at heads of Creeks 1 and 3 (d). Vertical lines indicate when flow reversals occurred in (b). Along channel water surface slopes during flood are into the marsh (i.e., creekmouth higher than creek head) and out of the marsh during ebb (i.e., creekmouth is lower than creek head). Cross marsh water surface slopes during the rising limb of the tide are from Creek 1 to Creek 3, and from Creek 3 to Creek 1 during the falling limb. The data are ensemble-averaged according to grouping; Neap tide (Tidal Amplitude <0.8 m.a.s.l.), Intermediate tide (0.8 < Tidal Amplitude <1.15 m.a.s.l.), and Spring tide (Tidal Amplitude >1.15 m.a.s.l.). Low marsh (LM), high marsh (HM), and MHHW are indicated in (a). Note that the scale in the y-axis in (c) increases from left to right (neap to spring) and is different in the left panel of (b).

3.1.2. Intermediate Tides (0.8 < Tidal Amplitude < 1.15 m.a.m.s.l.)

A different pattern among tidal creeks emerged between the Intermediate and Neap tides. In all creeks, the inflow gradually increased until the water level was between 0.72 and 0.82 m.a.s.m.l., or as the marsh platform flooded (center panel in Figure 4). However, for the remainder of the infilling period (1–2 h) Creek 1 inflows rapidly diminished and were 0.02 m/s at high water. Creek 3 displayed peak inflow of 0.39 m/s, which was 2.1 times greater than at Creek 1 and 1.2 times greater than at Creek 2. Following the peak inflow, Creek 3 displayed the same diminishment of inflow (i.e., no/minimal inflow at high water) as Creek 1. Conversely, Creek 2 displayed higher inflows (~0.10 m/s) and did not reverse until 26 min after high water. On average, Creek 2 flooded for ~40 min longer than Creeks 1 and 3 during the flood phase of the intermediate tide.

During the falling phase of the tide (red color in Figure 3), flows began to increase and peaked when the water surface elevation was below the creekbanks, that is, mostly channelized flow. Similar to the occurrence
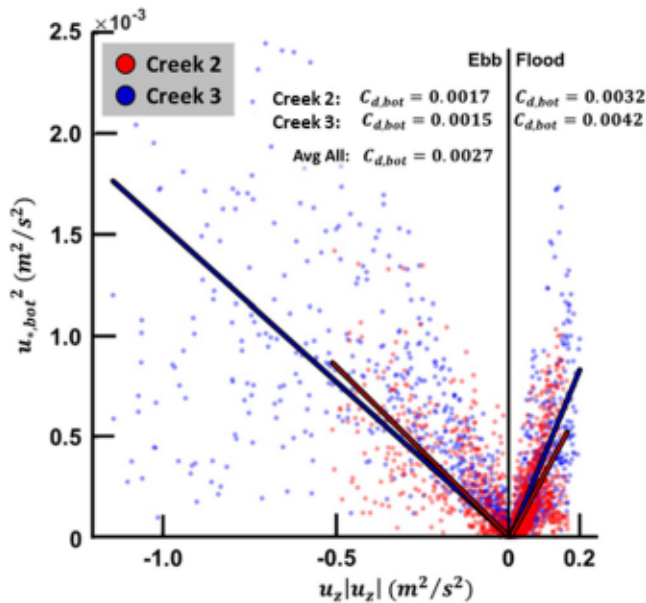
Figure 5. The balance between mean point-velocity measured (squared) at elevation z (x-axis) and the estimated shear velocity squared (y-axis) where the slope of the line represents the bed drag coefficient $C_{d,bot}$ for Creeks 2 and 3. The average $C_{d,bot}$ of both creeks and phases is 0.0027. Creek 1 is not included as the results were deemed unreliable for shear velocity estimates because of high variability.

of peak flooding due to rapid expansion of floodable area, peak ebbing occurred when the excess platform water can only exit the system through the creeks (i.e., no overbank flows). Creek 3 peak ebb velocity was on average −0.86 m/s (1.4 times greater than Creek 1 and 1.6 times greater than Creek 2). Creek 2 peaked approximately 25 and 10 min after Creeks 1 and 3, respectively.

3.1.3. Spring Tides (Tidal Amplitude > 1.15 m.a.m.s.l.)

The most notable changes to stage-velocity patterns occurred during the spring tides. During these tides, the high-water level exceeded the highest levees adjacent to Dean Creek, causing submergence of most, if not all, of the marsh surface in the study area (rightmost panels in Figure 4). The flooding pattern for Creek 1 was essentially the same as it was for intermediate tides, with the same peak flood velocity. Both Creeks 2 and 3 increased in peak flood velocities by 14% and 5%, respectively, relative to the intermediate tides. However, Creek 3 displayed slack water 65 min before high water, when the water level coincided with the highest levee elevations. As the water level continued to increase above the levee elevation, Creek 1 exhibited near-zero inflow and Creek 3 began to outflow. However, Creek 2 continued a sustained inflow (>0.15 m/s) until 30 min after high water (or as the water level began to recede). A water-level slope drove a cross-marsh flow from Creek 1 to Creek 3 (Figure 4d).

As the water level fell below the elevation of the highest levees, the stage-velocity relationship in all creeks was similar to the patterns in Intermediate tides. The outflow was the highest in all creeks when the flow was fully channelized. On average, the peak outflow for each creek was 0.82, 0.65, and 1.01 m/s, respectively, representing increases of 32% for Creek 1, 25% for Creek 2, and 17% for Creek 3, relative to peak ebb velocities in Intermediate tides. With respect to the peak flood to ebb velocity ratio, in all tides, all creeks showed stronger ebb velocities than flood velocities and are considered "ebb-dominated."

3.2. Bottom and Effective Drag in Intertidal Creeks

3.2.1. Bottom Drag Estimated From ADVs

Using Equations 5–7, the quadratic bottom drag coefficient was estimated throughout the 20 tide cycles in the data set (Figure 5), to be 0.0032 ($R^2 = 0.35$) on the flood phase and 0.0017 ($R^2 = 0.45$) for the ebb phase for Creek 2 (red). Similarly, the bottom drag in Creek 3 (blue) is 0.0042 ($R^2 = 0.58$) and 0.0015 ($R^2 = 0.54$) in the flood and ebb phases, respectively. Averaged across flood and ebb phases of all tides and across both creeks, the bottom drag is 0.0027 (SEM 6.40E−4) for z = 0.30 m above bed (canonical value = 0.0025). This value is comparable to that estimated by Voulgaris and Meyers (2004) of 0.0024 at z = 0.15 m above bed in a South Carolina, USA, salt marsh system located 300 km north of our study site with similar sediment and vegetation features. The estimated bed drag coefficient is used in subsequent estimates for velocity log-profile estimates, tidal discharge, and ultimately TSS fluxes for the measured time period.

3.2.2. Stage Varying Effective Drag

The effective drag is a measure of how much driving or restoring force is needed to produce a resultant flow; in other words, how much friction is resisting the flow. Shallow tidal embayments have long been recognized as systems dominated by friction (Friedrichs & Madsen, 1992; LeBlond, 1978; Rinaldo et al., 1999). Tidal waves in these systems can be represented as quasi-steady diffusive waves, where the local and advective accelerations (i.e., $\frac{\partial u_z}{\partial t}$ is $O(10^{-4})$) are much smaller than the pressure gradient and friction terms in the momentum balance (i.e., negligible terms on the left-hand side of Equation 7). Our measurements indicate that the pressure gradient and friction terms are both $O(10^{-3} \; to \; 10^{-2}$ m/s^2) in Creeks 2 and 3. These
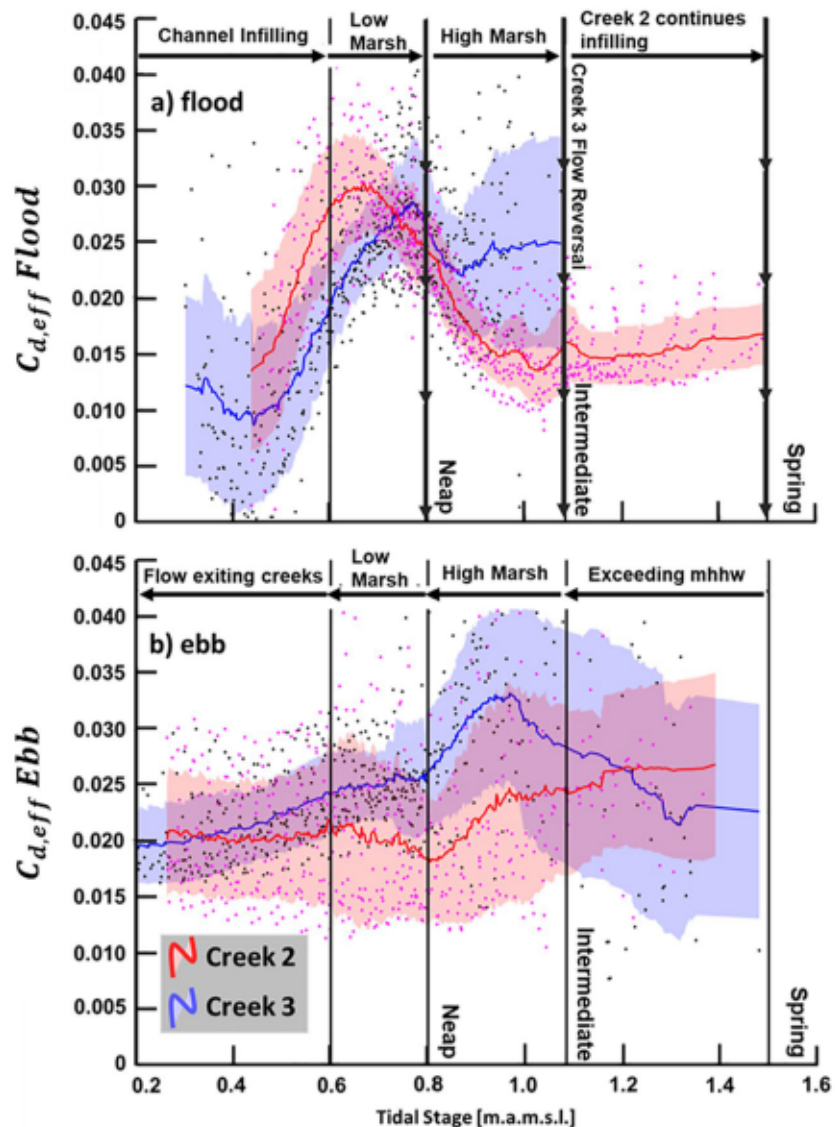
Figure 6. Effective drag (y-axis) plotted against tidal stage (x-axis) for Creeks 2 (red) and 3 (blue). The shaded area represents ±1 local standard deviation and the solid lines represent a moving average. Points indicate instantaneous values. Effective drag is separated by tidal stage such that panel (a) represents the flood, or rising limb, phase of the tide and panel (b) is the ebb, or falling limb of the tide. Single-headed arrows denote the direction to read the drag values over the course of a given tide, that is, left to right for flood in panel (a), and right to left for ebb in panel (b) In (a) effective drag increases as the tidal stage increases with the flood tide, and reaches a maximum between 0.6 and 0.8 m.a.m.s.l. in each creek, when flows begin spreading across low and high marsh elevations. After this maximum, Creek 2 drag reduces by 50%. Because Creek 3 inflows approach zero during spring tides, the drag cannot be properly evaluated (the denominator goes to zero), as expressed by no blue Creek 3 line being expressed at high tidal stages on the right of panel (a). During ebb (b), the graph is read from right to left, whereby Creek 2 effective drag decreases with tidal stage and approaches 0.02. Creek 3 effective drag increases before decreasing again to converge on 0.02. Note that the uncertainty during ebb (b) is considerably larger than during flood (a). Creek 1 data were not included in this as the results were sensitive to instrument vibrations.

values are between 1 and 2 orders of magnitude higher than found by French and Stoddart (1992) and Healy et al. (1981) in their respective field studies of tidal channels.

Estimates of the effective drag coefficient (Figure 6) ranged between 3 and 12 times greater than bed drag $\left(=0.0027\right)$ in Creeks 2 and 3. During the early stages of the flooding tide (Figure 6a), there is a minimum estimated drag in both creeks (=0.01–0.015) (note: the true minima likely occurs during the unmeasured

portion of flow). Equation 9 illustrates that when the water depth approaches zero, the hydraulic radius approaches zero, indicating that the total source of friction is from the bed (i.e., $C_{d,eff}$ / $C_{d,bot}$ → 1). However, because of the 20–30 cm height of our instruments, we were unable to directly measure this portion of the flow as the instruments were no longer submerged. As the stage increased, the drag coefficient increased and peaked at values of 0.03 and 0.028 for Creeks 2 and 3, respectively. These peaks occurred due to the expansion of floodable marsh area coinciding with the early stages of overmarsh flooding and the tide waters spreading across the platform (see average depth derived from Digital Elevation Model in Figure 2c). These values occurred when the water level was between 0.6 and 0.8 m.a.m.s.l. (i.e., low marsh elevations).

Following the maximum effective drag value, the drag declined in both creeks, corresponding to an average increase of water depth across the marsh as flood waters filled the marsh (Figure 2c). In Creek 3, because inflow velocities sharply fall during spring tides, as explained above and shown in Figure 2, the calculation for drag no longer yields realistic results (i.e., friction term becomes too small). This reduction of inflow, and early flow reversal, corresponded to a cross-marsh water surface gradient (from Creeks 1 and 2 to Creek 3; see Figure 4d). Conversely, the drag in Creek 2 approached a near constant value of 0.015 for tidal stages above 1.15 m.a.m.s.l., which corresponds to the mean higher high water elevation, or Dean Creek bank levee elevations (see Figure 2a). During the ebb phase (Figure 4b), for tidal stages greater than 0.8 m.a.m.s.l., there is increased uncertainty in the estimates for the drag due to variations in the water surface slope. However, both creeks converge to an effective drag of 0.020 when approaching 0.2 m.a.m.s.l. The effective drag estimates indicate that, over the duration of a tidal cycle, the drag from the landscape and vegetation effects is larger than bed drag, further supporting the results from Fagherazzi et al. (2008). Furthermore, the magnitude of the effective drag suggests that small (channel width <5 m) intertidal creeks can be treated as similar to steady-state systems, where the momentum balance is dominated by pressure gradient and friction terms, as found by previous works (Christiansen et al., 2000; Friedrichs & Madsen, 1992).

3.3. Tidal and TSS Transport and Directionality in Creeks

Understanding net transport with respect to water and TSS provides the necessary information to study the geospatial evolution and vertical accretion of marshes. The transport can be generally split into two modes; (a) tidal transport, or regular exchanges of flow and material due to tides and (b) episodic event-driven transport such as storm, rainfall, or wind events (Christiansen et al., 2000; Friedrichs & Perry, 2001; Hughes, 2012; Mariotti & Fagherazzi, 2011). Wind can influence both sediment transport and circulation patterns. Given sufficient water depth and fetch, wind waves can develop and resuspend sediments on the marsh platform (Callaghan et al., 2010). Furthermore, the composition of suspended particulates (i.e., increased organic material in the summer during peak plant productivity periods compared to winter) can vary throughout the year. During our sampling of TSS (7/29/2019), wind speeds were, on average, 2.9 m/s (STD 1.5 m/s) from the north (maximum measured wind speeds were 5.3 m/s).

Our findings (Figure 7) indicated that during neap tides, the net transport was essentially zero, or the same flow entered and exited the same creek. During neap tides, most if not all of the water, has been found to be transported through the channel sections (Bayliss-Smith et al., 1979; Bouma et al., 2005; Fagherazzi et al., 2008). However, for intermediate and spring tides, our estimates indicate that Creeks 1 and 3 have net outflows (negative net tidal transports), whereas Creek 2 shows net inflow. To result in a net transport, more water needs to exit the creek section rather than enter it, or vice versa. While a cross-marsh water-surface gradient (Figure 4d) occurred during intermediate and spring tides, and has the potential to be a contributing factor to the contrasting tidal flow asymmetries observed (Figure 6), it does not sufficiently explain this pattern.

In assessing the TSS flux for one measured tidal cycle (Figures 7b–7d), we found that Creek 1 was net exporting and Creeks 2 and 3 were net importing. The TSS fell at a faster rate for Creek 3 than Creeks 1 and 2 (Figure 7c), which corresponds to the extended low inflow/no inflow regime in Creek 3. Despite this, Creek 3 remained net importing for TSS due to the largest (of the three creeks) cross-sectional area, increased TSS concentrations, and greatest peak flood speeds.
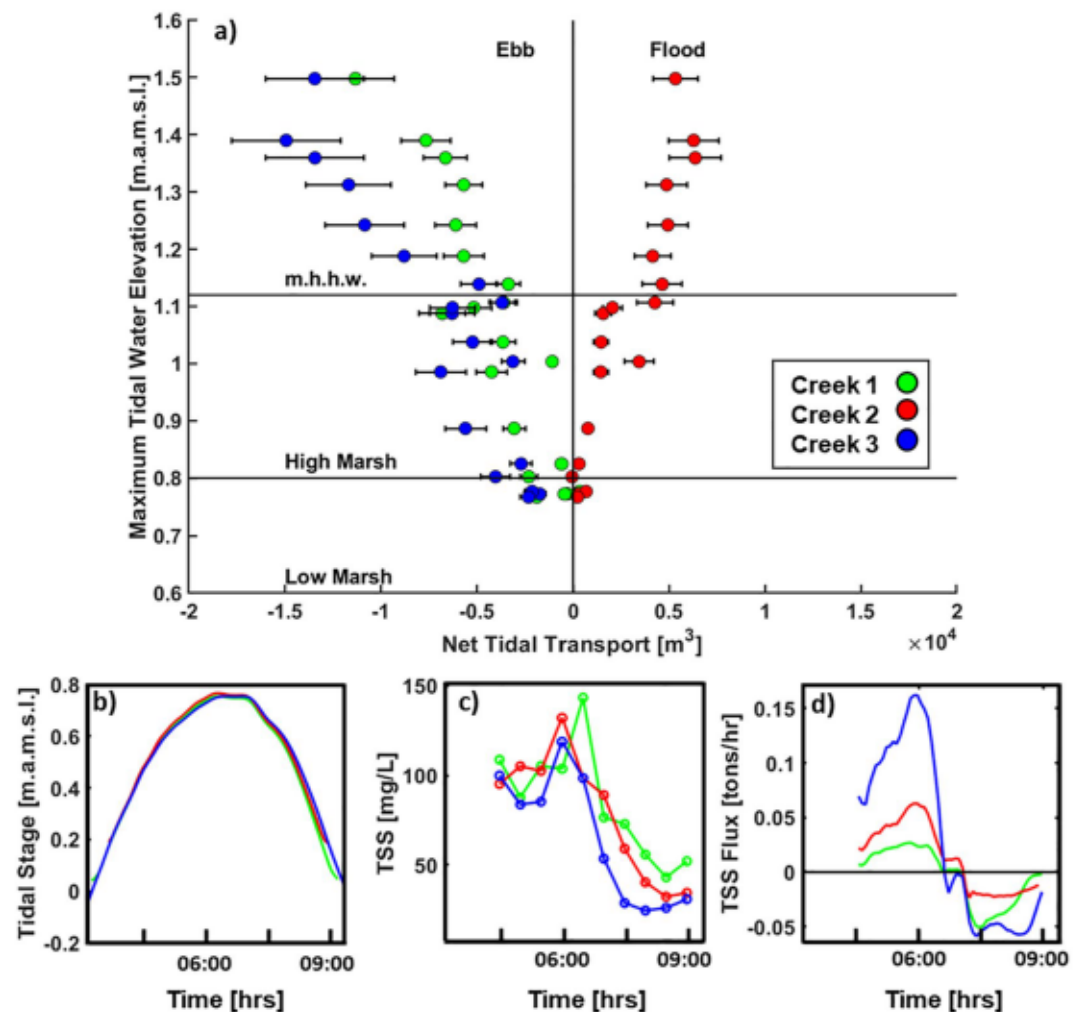
Figure 7. Estimated net tidal transport in each tidal creek for each tide of measured data versus maximum tidal elevation (a). Note that for neap tides (amplitude < 0.8), it is assumed that the exchange should be essentially zero, that is, water entering an individual creek exits through the same creek, however, the measurement period does not cover the entire tide. Tidal stage at each creek for the sampling period of total suspended sediments (TSS; b), TSS values during the course of the measured tide (c), and the estimated TSS flux (d).

4. Discussion

4.1. Potential Role of Tidal Meander Influencing Creek Flow Patterns

While there were no measurements of flow along Dean Creek, our data collected in the smaller creeks suggest that Dean Creek may alter the stage-velocity relationships, and ultimately drive creek-to-creek flow interactions, overmarsh circulation, and contrasting tidal flow asymmetries (flood/ebb differences) that were identified. Figure 4 illustrates the relative magnitude of velocity in each creek, the cross-marsh gradient direction, and the development of overbank flow for different times during intermediate and spring tides. Torres et al. (2007) presented an idealized representation of flooding in their study system, whereby the water propagates along the tidal channels in early stages of flood (similar to that found by additional authors [French & Stoddart, 1992; Friedrichs & Madsen, 1992; Hughes, 2012; LeBlond, 1978; Struyf et al., 2013]). Following their proposition (or portrayal), overbank flow begins as the channel levees are overtopped subsequently driving a circulation linked to the water-level slopes. The marsh in our study follows a consistent pattern, similar to Torres et al. (2007). However, the pattern is insufficient to explain the reduced inflow in Creek 1, seaward of Creek 2, during the flood tide. Creek 2 continued to display inflow beyond high water, for intermediate and spring tides, whereas Creek 1 inflows were not sustained (i.e., reduced close to 0 m/s).

This does not agree with the expectation that, since Creek 1 is closer to the ocean, the water surface elevation would be expected to be higher than that of Creek 2, thus continued inflows.

Two potential scenarios of tidal meander flow may contribute to the in-channel velocity flow patterns for each creek and in particular, for Creek 2: (a) water surface super-elevation near the confluence of Creek 2 during flood (enhance inflow of Creek 2) and ebb (suppress outflow); or (b) channel orientation and presence of bedforms in Dean Creek direct flow toward the bank which is nearly coincident with Creek 2 confluence and perpendicular to Creeks 1 and 3. These two scenarios are explored further in Sections 4.1.1 and 4.1.2.

4.1.1. Meander Super-elevations and Their Influence on Tidal Creek Velocities

The inflow reduction at Creek 1 and continued and sustained inflow at Creek 2 during the flood tide could be a super-elevation at the outer bend on Dean Creek, near the confluence of Creek 2 and Dean Creek (Figures 1, 2 and 7). Bend super elevations, or a lateral setup on the outer bend and set-down on the inner bend of a meander, develop through centrifugal accelerations (e.g, Blanckaert & De Vriend, 2003; Dietrich & Smith, 1983; Seminara, 2006). When water flows around bends, centrifugal force redistributes momentum laterally across the channel, leading to a water surface setup on the outerbend. This causes an imbalance in pressure gradient that drives a secondary flow consisting of surface flow toward the outer bend and near-bed flow toward the inner bend (Blanckaert & De Vriend, 2003; Dietrich & Smith, 1983; Seminara, 2006).

Recently, Kranenburg et al. (2019) measured tidal meander bend super elevations in a New England salt marsh in a weakly stratified tidal channel ($\frac{Channel\ Width}{Radius\ of\ Curvature} = 0.7$ in their study, our study $\frac{Channel\ Width}{Radius\ of\ Curvature} = 0.8$ at the confluence of Dean Creek and Creek 2). During maximum flood and ebb of a spring tide, they measured a ~3 cm cross-channel setup. During flood, the outer bend water surface elevation was 0.1 cm lower than the upstream location whereas the downstream segment (of approximately similar length) was 2.4 cm lower than the apex. Between Creeks 1 and 2, we measured an along channel (Dean Creek) water surface difference of 1–2 cm (Creek 2 higher than Creek 1) during the flooding phase (data not shown). This finding was contradictory to our initial expectation that Creek 1 would consistently exhibit higher water surface elevations during the flood phase as a result of its closer proximity to Doboy Sound relative to Creek 2. Furthermore, at peak ebb, Kranenburg et al. (2019) found that the outer bend water surface elevation was 0.8 and 3.4 cm higher than the upstream and downstream locations. This may provide insight as to why Creek 2 has a suppressed peak outflow when compared to Creeks 1 and 3 (26% less than Creek 1 and 55% less than Creek 3), as the bend super-elevation has the potential to suppress the allowable along-channel water surface gradient during ebb.

4.1.2. Influence of Flow Fields Altered by Large Bedforms in Main Channel on Tidal Creek Velocities

Another equally possible mechanism for the extended flooding of Creek 2 and inhibited outflow, could be the flow field alterations in Dean Creek caused by bedforms (highlighted in gray in the schematic in Figure 8). Recently, Finotello et al. (2020) demonstrated through a field study, the role that three-dimensional flow in tidal meanders has in shaping the morphodynamic evolution of microtidal meandering channels. They deployed acoustic Doppler current profilers (ADCPs) at three different tidal meander types near Venice Lagoon to measure the three-dimensional flow fields (translating asymmetric, straightening cuspate, and symmetric expansion—further details of these meander types can be found in Ahnert, 1960 and Finotello et al., 2020). The most similar meander they measured compared to the bend located near Creek 2 confluence was the translating asymmetric case ($\frac{Channel\ Width}{Radius\ of\ Curvature} = 0.85$ in their study, our study $\frac{Channel\ Width}{Radius\ of\ Curvature} = 0.8$ at confluence of Dean Creek and Creek 2). From the ADCP transect measurements located near the apex of the bend for this case, they found that during flood, the outer half of the bend had a primary velocity landward (i.e., preferential to flooding) and the inner bend near zero. However, on ebb, the inner bank had a primary seaward direction and the outer bank had a primary landward direction (i.e., recirculation eddy formed). The effect of this rotating cell would be that it would inhibit outflow
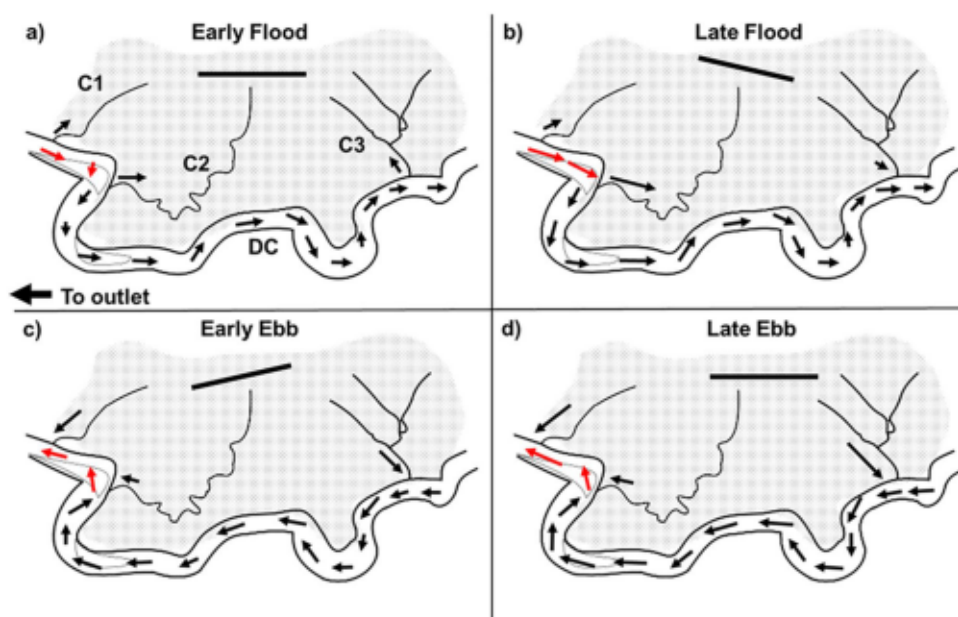
Figure 8. Schematic depicting flow patterns during flooding and ebbing tides in a intermediate/spring tide. Arrows represent general flow directions (assumed for Dean Creek) and red arrows indicate area of potential meander super-elevation influence or flow redirection from large bedforms. The solid bar on the marsh platform (patched area) indicates the cross-marsh water surface slope direction. (a) represents the site during early flood, (b) late flood, (c) early ebb, and (d) late ebb. Bed forms in main channel indicated in gray derived from aerial imagery at low tide.

if there were a connected intertidal creek with confluence nearby (i.e., potentially Creek 2 confluence with Dean Creek).

4.2. Outlook for Marsh Flows and Transport

While our field measurements were limited to only the intertidal creeks that connect to the main channel, future field studies have the potential to resolve these unknown linkages between marsh topography (i.e., overmarsh circulation and connectivity) (French & Stoddart, 1992; Meire et al., 2005; Sullivan et al., 2019; Torres & Styles, 2007), intertidal creek characteristics (Christiansen et al., 2000; Friedrichs & Madsen, 1992; Hughes, 2012; Mariotti & Fagherazzi, 2011; Pieterse et al., 2015, 2017), and main channel flow fields (Blanckaert & De Vriend, 2003; Bo & Ralston, 2020; Kranenburg et al., 2019). Furthermore, this work suggests that the TIGER model (Rinaldo et al., 1999) may have the potential to capture these differences in net exchanges between creeks if the boundary conditions are coupled with more detailed flow measurements within the main channel (i.e., dynamic water level and velocity boundary conditions). Additionally, future studies could evaluate the effective drag stage relationship in other creek systems. If found similar, this could provide a useful relationship for numerical study validations where measurements may be lacking due to accessibility or availability. We suggest future work utilize ADCPs to capture the vertical variability in tidal creek velocities, which would provide more accurate estimates of tidal transport.

5. Conclusions

Our field measurements of flow in three small intertidal creeks over a spring-neap period revealed tidal transport asymmetries within a confined drainage area. We provide estimates of effective drag coefficients for small intertidal creeks, which exhibited similar magnitudes as found in sea grass beds and coral reefs. Furthermore, our measurements indicate regular exchanges of water between creeks and overmarsh circulation, similar to what was found in Torres et al. (2007). We suggest that main channel flow patterns (such as meander bend super-elevations or rotating cells at meander bends) may have a stronger effect on tidal stage-velocity asymmetries (and thus stage-transport) than previously recognized. Our findings also suggest

that significant heterogeneity in the delivery of suspended sediments and biological material may be driven by the creek-creek divergences in flow and sediment transport, and cross-marsh circulation, and that such feedbacks have the potential to influence salt marsh geomorphic evolution and response to sea-level rise.

Data Availability Statement

Data for this study are available at via Zenodo at the following link (https://doi.org/10.5281/zenodo.5206708).

References

Ahnert, F. (1960). Estuarine meanders in the Chesapeake Bay area. *Geographical Review*, *50*(3), 390–401. https://doi.org/10.2307/212282

Barbier, E., Hacker, S., Kennedy, C., Koch, E., Stier, A., & Silliman, B. (2011). The value of estuarine and coastal ecosystem services. *Ecological Monographs*, *81*(2), 169–193. https://doi.org/10.1890/10-1510.1

Bayliss-Smith, T. P., Healey, R., Lailey, R., Spencer, T., & Stoddart, D. R. (1979). Tidal flows in salt marsh creeks. *Estuarine and Coastal Marine Science*, *9*(3), 235–255. https://doi.org/10.1016/0302-3524(79)90038-0

Blanckaert, K., & De Vriend, H. J. (2003). Nonlinear modeling of mean flow redistribution in curved open channels. *Water Resources Research*, *39*(12), 1–14. https://doi.org/10.1029/2003WR002068

Blanton, B. O., Werner, F. E., Seim, H. E., Luettich, R. A., Lynch, D. R., Smith, K. W., et al. (2004). Barotropic tides in the South Atlantic Bight. *Journal of Geophysical Research*, *109*(12), 1–17. https://doi.org/10.1029/2004JC002455

Bo, T., & Ralston, D. K. (2020). Flow separation and increased drag coefficient in estuarine channels with curvature. *Journal of Geophysical Research: Oceans*, *125*(10), 1–25. https://doi.org/10.1029/2020JC016267

Boon, J. D. (1975). Tidal discharge asymmetry in a salt marsh drainage system. *Limnology and Oceanography*, *20*(1), 71–80. https://doi.org/10.4319/lo.1975.20.1.0071

Bouma, T. J., Govers, G., Lauwaet, D., & Temmerman, S. (2005). Flow paths of water and sediment in a tidal marsh: Relations with marsh developmental stage and tidal inundation height. *Estuaries*, *28*(3), 338–352. https://doi.org/10.1007/BF02693917

Bouma, T. J., van Belzen, J., Balke, T., Zhu, Z., Airoldi, L., Blight, A. J., et al. (2014). Identifying knowledge gaps hampering application of intertidal habitats in coastal protection: Opportunities & steps to take. *Coastal Engineering*, *87*, 147–157. https://doi.org/10.1016/j.coastaleng.2013.11.014

Callaghan, D. P., Bouma, T. J., Klaassen, P., van der Wal, D., Stive, M. J. F., & Herman, P. M. J. (2010). Hydrodynamic forcing on salt-marsh development: Distinguishing the relative importance of waves and tidal flows. *Estuarine, Coastal and Shelf Science*, *89*(1), 73–88. https://doi.org/10.1016/j.ecss.2010.05.013

Christiansen, T., Wiberg, P. L., & Milligan, T. G. (2000). Flow and sediment transport on a tidal salt marsh surface. *Estuarine, Coastal and Shelf Science*, *50*(3), 315–331. https://doi.org/10.1006/ecss.2000.0548

Coverdale, T. C., Altieri, A. H., Bertness, M. D., & Kotanen, P. M. (2012). Belowground herbivory increases vulnerability of New England salt marshes to die-off. *Ecology*, *93*(9), 2085–2094. https://doi.org/10.1890/12-0010.1

Dietrich, W. E., & Smith, J. D. (1983). Influence of the point bar on flow through curved channels. *Water Resources Research*, *19*(5), 1173–1192. https://doi.org/10.1029/WR019i005p01173

Dyer, K. R. (1971). Current velocity profiles in a tidal channel. *Geophysical Journal of the Royal Astronomical Society*, *22*(2), 153–161. https://doi.org/10.1111/j.1365-246X.1971.tb03589.x

Fagherazzi, S., Hannion, M., & D'Odorico, P. (2008). Geomorphic structure of tidal hydrodynamics in salt marsh creeks. *Water Resources Research*, *44*(2), 1–12. https://doi.org/10.1029/2007WR006289

Fagherazzi, S., Kirwan, M. L., Mudd, S. M., Guntenspergen, G. R., Temmerman, S., D'Alpaos, A., et al. (2012). Numerical models of salt marsh evolution: Ecological, geomorphic, and climatic factors. *Reviews of Geophysics*, *50*(1), 1–28. https://doi.org/10.1029/2011RG000359

Feddersen, F., Gallagher, E. L., Guza, R. T., & Elgar, S. (2003). The drag coefficient, bottom roughness, and wave-breaking in the nearshore. *Coastal Engineering*, *48*(3), 189–195. https://doi.org/10.1016/S0378-3839(03)00026-7

Finotello, A., Ghinassi, M., Carniello, L., Belluco, E., Pivato, M., Tommasini, L., & D'Alpaos, A. (2020). Three-dimensional flow structures and morphodynamic evolution of microtidal meandering channels. *Water Resources Research*, *56*(7), 1–22. https://doi.org/10.1029/2020WR027822

Finotello, A., Lanzoni, S., Ghinassi, M., Marani, M., Rinaldo, A., & D'Alpaos, A. (2018). Field migration rates of tidal meanders recapitulate fluvial morphodynamics. *Proceedings of the National Academy of Sciences of the United States of America*, *115*(7), 1463–1468. https://doi.org/10.1073/pnas.1711330115

French, J. R., & Stoddart, D. R. (1992). Hydrodynamics of salt marsh creek systems: Implications for marsh morphological development and material exchange. *Earth Surface Processes and Landforms*, *17*(3), 235–252. https://doi.org/10.1002/esp.3290170304

Friedrichs, C. T., & Madsen, O. S. (1992). Nonlinear diffusion of the tidal signal in frictionally dominated embayments. *Journal of Geophysical Research*, *97*(C4), 5637. https://doi.org/10.1029/92jc00354

Friedrichs, C. T., & Perry, J. E. (2001). Tidal salt marsh morphodynamics. *Journal of Coastal Research*, *27*(27), 6–36.

Goring, D. G., & Nikora, V. I. (2002). Despiking acoustic doppler velocimeter data. *Journal of Hydraulic Engineering*, *128*(1), 117–126. https://doi.org/10.1061/(ASCE)0733-942910.1061/(asce)0733-9429(2002)128:1(117)

Grant, W. D., & Madsen, O. S. (1982). Movable bed roughness in unsteady oscillatory flow. *Journal of Geophysical Research*, *87*(C1), 469–481. https://doi.org/10.1029/JC087iC01p00469

Healey, R. G., Pye, K., Stoddart, D. R., & Bayliss-Smith, T. P. (1981). Velocity variations in salt marsh creeks, Norfolk, England. *Estuarine, Coastal and Shelf Science*, *13*(5), 535–545. https://doi.org/10.1016/S0302-3524(81)80056-4

Horstman, E. M., Bryan, K. R., & Mullarney, J. C. (2021). Drag variations, tidal asymmetry and tidal range changes in a mangrove creek system. *Earth Surface Processes and Landforms*, *46*, 1–1846. https://doi.org/10.1002/esp.5124

Hughes, Z. J. (2012). Tidal channels on tidal flats and marshes BT. In R. A. Davis Jr. & R. W. Dalrymple (Eds.), *Principles of tidal sedimentology* (pp. 269–300). Springer Netherlands. https://doi.org/10.1007/978-94-007-0123-6_11

Kim, S.-C., Friedrichs, C. T., Maa, P.-Y., & Wright, D. L. (2000). Estimating bottom stress in tidal boundary layer from acoustic doppler velocimeter data. *Journal of Hydraulic Engineering*, *126*(6), 399–406. https://doi.org/10.1061/(ASCE)0733-9429

Kranenburg, W. M., Geyer, W. R., Garcia, A. M. P., & Ralston, D. K. (2019). Reversed lateral circulation in a sharp estuarine bend with weak stratification. *Journal of Physical Oceanography*, *49*(6), 1619–1637. https://doi.org/10.1175/JPO-D-18-0175.1

LeBlond, P. H. (1978). On tidal propagation in shallow rivers. *Journal of Geophysical Research*, *83*(C9), 4717. https://doi.org/10.1029/jc083ic09p04717

Li, C., Valle-Levinson, A., Atkinson, L. P., Wong, K. C., & Lwiza, K. M. M. (2004). Estimation of drag coefficient in James River estuary using tidal velocity data from a vessel-towed ADCP. *Journal of Geophysical Research*, *109*(3). https://doi.org/10.1029/2003jc001991

Lin, Q., & Mendelssohn, I. A. (2012). Impacts and recovery of the deepwater horizon oil spill on vegetation structure and function of coastal salt marshes in the northern Gulf of Mexico. *Environmental Science and Technology*, *46*(7), 3737–3743. https://doi.org/10.1021/es203552p

Mariotti, G., & Fagherazzi, S. (2011). Asymmetric fluxes of water and sediments in a mesotidal mudflat channel. *Continental Shelf Research*, *31*(1), 23–36. https://doi.org/10.1016/j.csr.2010.10.014

Metre, P., Bouma, T. J., Tánczos, I. C., Kusters, L., van Regenmortel, S., Hesselink, A., et al. (2005). Flow hydrodynamics on a mudflat and in salt marsh vegetation: Identifying general relationships for habitat characterisations. *Hydrobiologia*, *540*(1–3), 259–274. https://doi.org/10.1007/s10750-004-7149-0

Monismith, S. G. (2007). Hydrodynamics of coral reefs. *Annual Review of Fluid Mechanics*, *39*, 37–55. https://doi.org/10.1146/annurev.fluid.38.050304.092125

Monismith, S. G., Hirsh, H., Batista, N., Francis, H., Egan, G., & Dunbar, R. B. (2019). Flow and drag in a seagrass bed. *Journal of Geophysical Research: Oceans*, *124*(3), 2153–2163. https://doi.org/10.1029/2018JC014862

Nepf, H. M. (1999). Drag, turbulence, and diffusion in flow through emergent vegetation. *Water Resources Research*, *35*(2), 479–489. https://doi.org/10.1029/1998WR900069

Nidzieko, N. J., & Ralston, D. K. (2012). Tidal asymmetry and velocity skew over tidal flats and shallow channels within a macrotidal river delta. *Journal of Geophysical Research*, *117*(3). https://doi.org/10.1029/2011JC007384

Nikuradse, J., & VDI, V. (1933). *Strömungsgesetze in rauhen Rohren*.

Office for Coastal Management. (2010). *Coastal Georgia Elevation Project Lidar Data from 2010-06-15 to 2010-08-15*. NOAA National Centers for Environmental Information. Retrieved from https://www.fisheries.noaa.gov/inport/item/48167

Pieterse, A., Puleo, J. A., Mckenna, T. E., & Aiken, R. A. (2015). Near-bed shear stress, turbulence production and dissipation in a shallow and narrow tidal channel. *Earth Surface Processes and Landforms*, *40*(15), 2059–2070. https://doi.org/10.1002/esp.3782

Pieterse, A., Puleo, J. A., Mckenna, T. E., & Figlus, J. (2012). In situ measurements of shear stress, erosion and deposition in man-made tidal channels within a tidal saltmarsh. *Estuarine, Coastal and Shelf Science*, *192*, 29–41. https://doi.org/10.1016/j.ecss.2017.04.028

Pieterse, A., Puleo, J. A., McKenna, T. E., & Figlus, J. (2017). In situ measurements of shear stress, erosion and deposition in man-made tidal channels within a tidal saltmarsh. *Estuarine, Coastal and Shelf Science*, *192*, 29–41. https://doi.org/10.1016/j.ecss.2017.04.028

Pinton, D., Canestrelli, A., Wilkinson, B., Ifju, P., & Ortega, A. (2020). A new algorithm for estimating ground elevation and vegetation characteristics in coastal salt marshes from high-resolution UAV-based LiDAR point clouds. *Earth Surface Processes and Landforms*, *45*(14), 3687–3701. https://doi.org/10.1002/esp.4992

Rantz, S. E. (1982). *Measurement and computation of streamflow*. Water Supply Paper 1 & 2. https://doi.org/10.3133/wsp2175

Rinaldo, A., Fagherazzi, S., Lanzoni, S., Marani, M., & Dietrich, W. E. (1999). Tidal networks: 2. Watershed delineation and comparative network morphology. *Water Resources Research*, *35*(12), 3905–3917. https://doi.org/10.1029/1999WR900237

Rusello, P. (2009). *A practical primer for pulse coherent instruments* (Nortek Technical Note No.: TN-027, pp. 1–17). Retrieved from http://scholar.google.com/scholar?hl=en&btnG=Search&q=intitle:A+Practical+Primer+for+Pulse+Coherent+Instruments#0

Seminara, G. (2006). Meanders. *Journal of Fluid Mechanics*, *554*, 271–297. https://doi.org/10.1017/S0022112006008925

Soulsby, R. L. (1983). Chapter 5—The bottom boundary layer of shelf seas. In B. B. T.-E. O. S. Johns (Ed.), *Physical oceanography of coastal and shelf seas* (Vol. 35, pp. 189–266). Elsevier. https://doi.org/10.1016/S0422-9894(08)70503-8

Struyf, E., Temmerman, S., Fagherazzi, S., Wiberg, P. L., Raymond, P. A., & Zhao, Y. (2013). Fluxes of water, sediments, and biogeochemical compounds in salt marshes. *Ecological Processes*, *2*(1), 1–16. https://doi.org/10.1186/2192-1709-2-3

Sullivan, J. C., Torres, R., & Garrett, A. (2019). Intertidal creeks and overmarsh circulation in a small salt marsh basin. *Journal of Geophysical Research: Earth Surface*, *124*(2), 447–463. https://doi.org/10.1029/2018JF004861

Temmerman, S., Bouma, T. J., Govers, G., & Lauwaet, D. (2005). Flow paths of water and sediment in a tidal marsh: Relations with marsh developmental stage and tidal inundation height. *Estuaries*, *28*(3), 338–352. https://doi.org/10.1007/BF02693917

Temmerman, S., Metre, P., Bouma, T. J., Herman, P. M. J., Ysebaert, T., & De Vriend, H. J. (2013). Ecosystem-based coastal defence in the face of global change. *Nature*, *504*(7478), 79–83. https://doi.org/10.1038/nature12859

Torres, R., & Styles, R. (2007). Effects of topographic structure on salt marsh currents. *Journal of Geophysical Research: Earth Surface*, *112*(2), 1–14. https://doi.org/10.1029/2006JF000508

Voulgaris, G., & Meyers, S. T. (2004). Temporal variability of hydrodynamics, sediment concentration and sediment settling velocity in a tidal creek. *Continental Shelf Research*, *24*(15), 1659–1683. https://doi.org/10.1016/j.csr.2004.05.006

Voulgaris, G., & Trowbridge, J. (1998). Evaluation of the Acoustic Doppler Velocimeter (ADV) for turbulence measurements. *Journal of Atmospheric and Oceanic Technology*, *15*(1), 272–289. https://doi.org/10.1175/1520-0426(1998)015<0272:eotadv>2.0.co;2

Walker, J. F. (1988). General two-point method for determining velocity in open channel. *Journal of Hydraulic Engineering*, *114*(7), 801–805. https://doi.org/10.1061/(asce)0733-9429(1988)114:7(801)

Warner, S. J., & MacCready, P. (2014). Headland: Internal waves versus eddies. *Journal of Geophysical Research: Oceans*, *119*, 1554–1571. https://doi.org/10.1002/2013JC009757.Received

Yen, B. C. (2002). Open channel flow resistance. *Journal of Hydraulic Engineering*, *128*(1), 20–39. https://doi.org/10.1061/(asce)0733-9429